RSC Advances

PAPER

View Article Online
View Journal | View Issue

Cite this: *RSC Adv.*, 2024, **14**, 10255

Rigidify styryl-pyridinium dyes to benzo[*h*] coumarin-based bright two-photon fluorescent probes for cellular bioimaging†

Chengjing Zhang,[a] Zihao Yu,[b] Yang Liu,[a] Wendong Jin,[a] Zhiqiang Liu *[a] and Xiaoqiang Yu *[a]

Received 4th December 2023
Accepted 23rd March 2024

DOI: 10.1039/d3ra08269e

rsc.li/rsc-advances

Fluorescence imaging of organelles at the cellular level is important for studying biological processes. The development of a highly emissive fluorescent probe that operates under a suitable excitation light source is a key step in high-quality fluorescence imaging. For long-term, high-fidelity fluorescence imaging of mitochondria-related cellular processes using two-photon microscopy and stimulated emission depletion microscopy, we developed a new benzocoumarin-based cationic fluorescent probe (**BS-CN**) that is far-red emitting, water-soluble, photostable, and very bright in cells. **BS-CN** showed a remarkably high quantum yield of 0.35 and a large two-photon excited fluorescence action cross-section of 76 GM, enabling the long-term tracking of mitochondria in live cells. In addition, **BS-CN** exhibited a certain affinity for RNA and stained nucleoli in fixed cells. A comparative assessment of the photophysical properties and bioimaging performance of benzo[*h*]coumarin-pyridinium and the structurally similar styryl-pyridinium (**BS-MN**) clearly indicated the importance of structural rigidity for fluorescence efficiency.

1. Introduction

Fluorescence imaging techniques combined with probes with target selectivity provide powerful tools for biological research.[1,2] To enhance the quality and resolution of microscopic images, many revolutionary microscopy techniques, such as confocal laser scanning microscopy (CLSM), two-photon laser microscopy, and stimulated emission depletion (STED) microscopy, have been developed.[3–5] Generally, these types of microscopy require highly emissive fluorescent probes to label the target and thereby to realize high-quality fluorescence imaging.[6]

Organic fluorescent probes have become increasingly popular owing to their unique advantages, such as good biocompatibility, simple preparation process, low molecular weight, and relatively quick responses.[7,8] The luminescence performance and function of probes can be easily tuned by adjusting the molecular structures to meet various requirements.[9,10] Many important low-molecular-weight organic fluorescent probes have been developed and commercialized.[11] For example, fluorescent probes have been used to identify cancer-related markers, observe the interactions and dynamic changes between organelles in real time, and detect changes in the cell microenvironment (such as polarity, viscosity, and pH).[12–15]

Mitochondria are membrane-bound organelles that are abundant in the cytoplasm of eukaryotic cells and play important roles in all biological processes (*e.g.*, by generating the chemical energy needed to power biochemical reactions, participating in cell proliferation, and regulating programmed cell death).[16–18] Mitochondria are morphologically diverse organelles with substantial variation in size and shape, ranging from small particles to highly filamentous structures.[19] Changes in mitochondrial morphology are believed to be closely related to some degenerative diseases in humans, such as Parkinson's disease, Alzheimer's disease, and amyotrophic lateral sclerosis.[20] Thus, long-term and high-fidelity visualization and tracking are valuable to understand the roles of mitochondria.

Many mitochondrial fluorescent probes have been developed and applied to record and track the dynamic changes in mitochondria in living cells.[21–23] The transmembrane potential of the inner membrane is as high as −180 mV, which distinguishes mitochondria from other organelles.[24,25] Therefore, designing probes with a positive charge to target mitochondria is an efficient strategy. Most commercial mitochondrial trackers and conventional mitochondrial probes, either reaction-free or reaction-based, have a cationic moiety that utilizes electrostatic attraction and enhances the targeting affinity to mitochondria.[26–29] However, the quantum yields of styryl-pyridinium dyes are generally low.[25,27–29] In addition, the nucleolus is an important component of the cell nucleus, and its morphology is related to neurodegenerative diseases, such as

[a]*State Key Laboratory of Crystal Materials, Shandong University, Jinan 250100, China. E-mail: zqliu@sdu.edu.cn; yuxq@sdu.edu.cn*

[b]*School of Material Science and Engineering, Wuhan University of Technology, Wuhan 430070, China*

† Electronic supplementary information (ESI) available. See DOI: https://doi.org/10.1039/d3ra08269e

Parkinson's disease.[30] Recent reports have found that many probes could enter the nucleolus due to the disappearance of the mitochondrial membrane potential.[25,31] This facilitates the detection of mitochondrial damage and can be used for analyses of nucleolar morphology in fixed cells.

To fully utilize the advantages of advanced microscopy (*e.g.*, TPM (two-photon microscopy) and STED), such as the high spatial and temporal resolution, non-destructive operation, and long-term time-lapse imaging, the probes must be suitable for far-red emission, sufficient photostability, large nonlinear absorption, compatibility with the excitation laser, and brightness in cells.[32–34] Our group has developed a number of fluorescent mitochondrial probes based on the styryl-pyridinium platform with an ultrahigh signal-to-noise ratio and excellent leakage-free performance.[35–38] In this study, we designed and synthesized a fluorescent probe for specifically targeting mitochondria for a long time and successfully stained the nucleolus of fixed cells. A comparative study of the photophysical properties and bioimaging performance of benzo[*h*]coumarin-pyridinium (**BS-CN**) and a structurally similar styryl-pyridinium (**BS-MN**) was carried out to determine the importance of structural rigidity for fluorescence efficiency. **BS-CN** exhibited a remarkably high quantum yield of 35.6%, a large two-photon excited fluorescence (TPEF) action cross-section ($\delta \times \Phi$) of 76 GM under 900 nm laser excitation, efficient photostability, and compatibility with a 775 nm STED laser. This probe could be used to obtain images of mitochondria without washing at a low concentration of 500 nM with low phototoxicity, avoiding the measurement error caused by self-quenching and auto-fluorescence due to its large Stokes shift (compared with the absorption spectrum, the fluorescence spectrum has a redshift of up to 169 nm), far-red emission, and excellent brightness.

2. Experimental section

2.1. Materials and instruments

Materials and instruments are described in ESI.†

2.2. Synthesis of probes

The synthetic routes of **BS-MN** and **BS-CN** are shown in Scheme 1,[39,40] and characterization data are shown in ESI (Fig. S8 and S19†).

2.2.1 Synthesis of 6-(dimethylamino)-1-methoxy-2-naphthaldehyde (compound 2). The starting material 6-(dimethylamino)-1-hydroxy-2-naphthaldehyde was synthesized as reported in the literature.[9] 6-(Dimethylamino)-1-hydroxy-2-naphthaldehyde (1.08 g, 5 mmol), K_2CO_3 (1.04 g, 7.5 mmol) and CH_3I (1.06 g, 7.5 mmol) were added to DMF (10 mL) in a round bottomed flask, and the mixture was stirred at room temperature for 4 h. Then, the solvent was removed under reduced pressure, and the residue was purified by silica gel chromatography ($V_{hexane}/V_{ethylacetate}$ = 8 : 1 to 3 : 1) to give compound as a bright yellow solid (840 mg, 73% yield based on 6-(dimethylamino)-1-hydroxy-2-naphthaldehyde). ^{1}H NMR (400 MHz, DMSO-d_6), δ (ppm): 10.32 (d, J = 6.4 Hz, 1H), 8.04 (d, J = 9.3 Hz, 1H), 7.58 (d, J = 8.7 Hz, 1H), 7.47 (d, J = 8.8 Hz, 1H), 7.29 (dd, J = 9.4, 2.6 Hz, 1H), 6.98 (d, J = 2.6 Hz, 1H), 4.06 (s, 3H), 3.09 (s, 6H). ^{13}C NMR (100 MHz, DMSO-d_6), δ (ppm): 188.75, 163.23, 151.25, 140.49, 124.78, 123.09, 123.04, 121.02, 119.03, 116.61, 106.02, 65.95, 40.32. HRMS (ESI) m/z calcd for $[C_{14}H_{16}NO_2^+]$ 230.1136 ($[M + H]^+$), found 230.1178.

2.2.2 Synthesis of 8-(dimethylamino)-3-(pyridin-4-yl)-2*H*-benzo[*h*]chromen-2-one (compound 3). 4-Pyridineacetonitrile (155 mg, 1 mmol) and *t*-BuOK (135 mg, 1.2 mmol) were added to anhydrous ethanol (20 mL) and stirred for 10 minutes. Then, 6-(dimethylamino)-1-hydroxy-2-naphthaldehyde (194 mg, 0.9 mmol) was added and stirred at 90 °C for 24 h. After cooling to room temperature, the solvent was removed under reduced pressure, the reaction mixture was extracted in acidic medium with ethyl acetate. Then, the organic layer was dried with anhydrous $MgSO_4$ for 2 h and evaporated under reduced pressure to remove the solvent. The residue was purified by silica gel chromatography (V_{DCM}/V_{MeOH} = 90 : 1 to 70 : 1) to give compound as a reddish brown solid (99 mg, 35% yield based on 6-(dimethylamino)-1-hydroxy-2-naphthaldehyde). ^{1}H NMR (400 MHz, DMSO-d_6), δ (ppm): 8.67 (dd, J = 4.6, 1.5 Hz, 2H), 8.57 (s, 1H), 8.23 (d, J = 9.3 Hz, 1H), 7.86 (dd, J = 4.6, 1.6 Hz, 2H), 7.61 (s, 2H), 7.38 (dd, J = 9.4, 2.5 Hz, 1H), 7.05 (d, J = 2.5 Hz, 1H), 3.12 (s, 6H). ^{13}C NMR (100 MHz, $CDCl_3$), δ (ppm): 160.34, 152.41, 150.68, 149.93, 142.96, 142.68, 137.60, 124.21, 123.94, 123.37, 122.47, 120.88, 115.96, 114.36, 111.67, 105.61, 40.34. HRMS (ESI) m/z calcd for $[C_{20}H_{17}N_2O_2^+]$ 317.1285 ($[M + H]^+$), found 317.1261.

2.2.3 Synthesis of BS-MN. 6-(Dimethylamino)-1-methoxy-2-naphthaldehyde (100 mg, 0.44 mmol) and 1-methyl-4-picolinium iodide (123 mg, 0.52 mmol) were added to anhydrous acetonitrile (8 mL), then added five drops of piperidine as a catalyst. The mixture was heated at 80 °C for 24 hours. Then, acetonitrile was removed under reduced pressure and the mixture was purified by silica gel chromatography (V_{DCM}/V_{MeOH} = 50 : 1) to give **BS-MN** as a brown solid (54 mg, 28% yield based on 6-(dimethylamino)-1-methoxy-2-naphthaldehyde). ^{1}H NMR (400 MHz, DMSO-d_6), δ (ppm): 8.79 (d, J = 6.8 Hz, 2H), 8.25 (d, J = 6.8 Hz, 2H), 8.15 (d, J = 16.4 Hz, 1H), 7.97 (d, J = 9.3 Hz, 1H), 7.80 (d, J = 8.9 Hz, 1H), 7.54–7.47 (m, 2H), 7.28 (dd, J = 9.3, 2.5 Hz, 1H), 7.00 (d, J = 2.4 Hz, 1H), 4.25 (s, 3H), 3.97 (s, 3H), 3.08 (s, 6H). ^{13}C NMR (100 MHz, DMSO-d_6), δ (ppm): 157.32, 153.33, 150.18, 145.25, 138.18, 135.26, 124.42, 124.12, 123.62, 123.46, 119.87, 119.85, 116.67, 106.42, 64.22, 47.19, 44.23. HRMS (ESI) m/z calcd for $[C_{21}H_{23}N_2O^+]$ 319.1805 ($[M–I]^+$), found 319.1794.

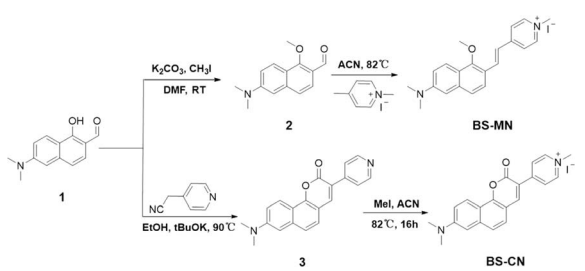

Scheme 1 Synthetic route of **BS-MN** and **BS-CN**.

2.2.4 Synthesis of BS-CN. 8-(Dimethylamino)-3-(pyridin-4-yl)-2*H*-benzo[*h*]chromen-2-one (165 mg, 0.52 mmol) and methyl iodide (0.6 mg, 4.23 mmol) in 1,4-dioxane (16 mL) was added into a Schlenk tube stirred at 95 °C for 15 h. After cooling to room temperature, a dark red precipitate was obtained by filtration using a filter flask. Then recrystallization from ethyl acetate led to crystals to give the compound **BS-CN** as a dark red solid (74 mg, 31% yield based on 8-(dimethylamino)-3-(pyridin-4-yl)-2*H*-benzo[*h*]chromen-2-one). ^{1}H NMR (400 MHz, methanol-d_4), δ (ppm): 8.83 (s, 1H), 8.80 (d, J = 6.9 Hz, 2H), 8.64 (d, J = 7.0 Hz, 2H), 8.33 (d, J = 9.4 Hz, 1H), 7.57–7.51 (m, 2H), 7.33 (dd, J = 9.4, 2.5 Hz, 1H), 7.00 (d, J = 2.5 Hz, 1H), 4.34 (s, 3H), 3.15 (s, 6H). ^{13}C NMR (100 MHz, DMSO-d_6), δ (ppm): 159.35, 153.47, 151.61, 150.64, 147.67, 145.33, 138.73, 125.53, 124.98, 123.98, 123.96, 116.82, 115.75, 113.17, 111.87, 106.12, 47.62, 40.32. HRMS (ESI) m/z calcd for $[C_{21}H_{19}N_2O_2^+]$ 331.1442 ([M–I]$^+$), found 331.1449.

2.3. Living cells culture

HeLa cells were cultured in the H-DMEM culture medium containing 10% fetal bovine serum (FBS) and 1% penicillin/streptomycin in an incubator containing 5% CO_2 at 37 °C for 36 h. Then, added the probes and Hoechst 33342 into the culture medium and incubated for 30 minutes and 10 minutes respectively. For co-localized imaging, we added the probes and MitoTracker Green into the culture medium and incubated for 30 minutes.

2.4. Fixed cell experiment

HeLa cells were fixed with cold 4% paraformaldehyde for 2.5 h, then washed away by PBS (phosphate buffer saline), and treated with 0.5% TritonX-100 for 5 min, after that washed with PBS. The cells were subsequently incubated with probes for 20 minutes. Subsequently, Hoechst 33342 (2 μM) was added and incubated for an additional 10 minutes before imaging. We fixed the cells in the same way, then treated with RNase (5 mg mL^{-1}) for 2 h. Finally, the cells were incubated with probes for 20 min, and Hoechst 33342 (2 μM) for 10 min before imaging.

2.5. Photostability

The cells were incubated with **BS-CN** (500 nM)/**BS-MN** (1 μM) for 30 min, and imaged by CLSM. By continuous scanning to extract pictures of 0, 10, 20, 30, 40 minutes.

2.6. Long-time tracking

The cells were incubated with **BS-CN** (500 nM)/**BS-MN** (1 μM) for 30 min, changed the culture medium every 36 h and imaged at 1 h, 15 h, 30 h, 45 h and 60 h.

2.7. pH experiment

Britton–Robison standard buffer solution (pH = 2) was diluted with NaOH solution to prepare the needed solutions with pH of 4, 5, 6, 7, 8 and 9. The pH value of the solution was checked using a pH meter. Then the probe was added into the solutions to measure the fluorescence intensity.

3. Results and discussion

3.1. Design and synthesis

In this study, we developed novel fluorescent probes that target mitochondria in living cells and stain fixed cells. We first designed **BS-MN**, which incorporated an electron-rich dialkylamino group as an electron-donating group (D) and an electron-withdrawing pyridinium as an electron-accepting group (A). We used styryl-naphthalene instead of styryl-benzene as a conjugated bridge (π) to extend the emission band to the deep-red and NIR region. This design resulted in excellent push–pull electronic effects within the molecular structure of D–π–A. Endogenous substances in cells may destroy the double bond structure in **BS-MN**, and the influence of the isomerization of carbon–carbon double bonds on the molecular structure as well as the increase in non-radiative transitions due to the rotation of a single bond led to a reduction in the fluorescence emission efficiency and strength of intracellular imaging. Therefore, we synthesized **BS-CN** by constructing a rigid ring *via* intramolecular esterification to enhance the fluorescence performance and stability of the probe. This effectively reduced the single-bond rotation within the molecule.

3.2. Photophysical properties

The absorption and emission spectra were measured in various solvents. As shown in Fig. 1, both **BS-CN** and **BS-MN** showed maximum absorbance at 470–510 nm and 474–490 nm, respectively. Emission peaks of **BS-CN** and **BS-MN** were observed at 650–670 nm and 655–685 nm, respectively. The optical properties of **BS-CN** and **BS-MN** in various solvents are listed in Table S1.† The probes exhibited large Stokes shifts of 117–169 nm for **BS-CN** and 126–221 nm for **BS-MN**. **BS-CN** showed higher molar extinction coefficients and fluorescence quantum yields than those of **BS-MN** in all tested solvents. As shown in Fig. 1E and G, **BS-CN** exhibited a more stable Stokes shift than that of **BS-MN** with changes in polarity. These results indicated that **BS-CN** possessed superior photophysical properties. Moreover, changes in intracellular polarity did not affect the imaging capability of the probe.

Meanwhile, we found that the fluorescence quantum yields of most reported styryl-pyridinium dyes were generally low,[25,27–29] and this resulted in staining only at a high concentration, which may cause damage to cells (Table S2†). We synthesized **BS-CN** with reasonable rigidity, which improved its molecular planarity and fluorescence quantum yield. Remarkably, the fluorescence quantum yield reached an astonishing 35.6%, allowing accurate mitochondrial imaging at a low concentration of 500 nM.

To study the effects of pH, the stability of **BS-CN** was investigated under different pH conditions (Fig. 1F and H). We found that **BS-CN** had almost no spectral change at pH 4.0–9.0; however, **BS-MN** had a little spectral change in pH 4.0–5.0 (Fig. S1†). This demonstrated that stability is higher for **BS-CN** than for **BS-MN** across a range of pH values.

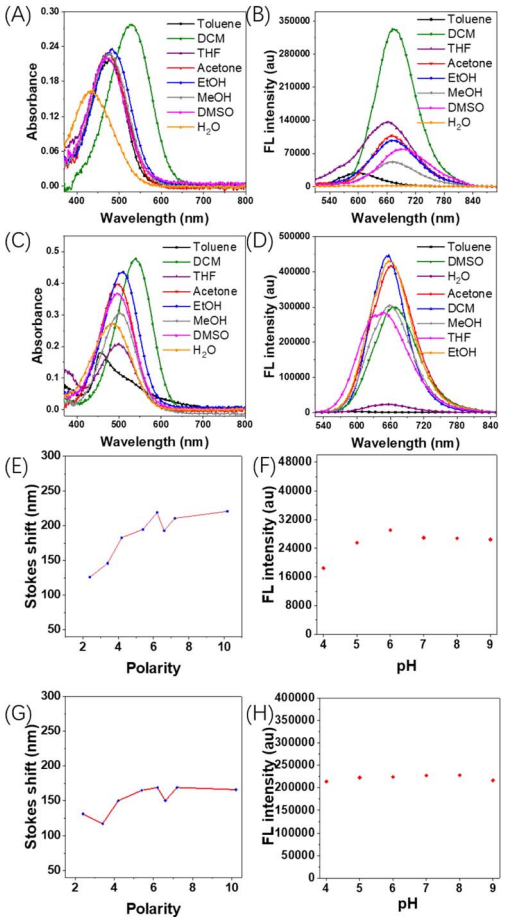

Fig. 1 Absorption and emission spectra of BS-MN (A and B) and BS-CN (C and D) in various solvents. Stokes shift of BS-MN (E) and BS-CN (G) in different polarities. Maximum fluorescence intensities of BS-MN (F) and BS-CN (H) in different pH solutions. Concentration: 10 μM, λ_{ex} = 488 nm. FL: fluorescence.

We investigated the two-photon properties of the probes using Rhodamine B as a reference. **BS-CN** and **BS-MN** had TPEF action cross-sections ($\delta \times \Phi$) of 76.7 GM and 7.9 GM (1 GM = 10^{-50} (cm^4 s) per photon) upon excitation at 1050 nm (Fig. S2†). These results demonstrate that **BS-CN** exhibits superior two-photon performance compared with those of **BS-MN** and similar previously reported compounds.[35]

3.3. Confocal fluorescence imaging

Prior to fluorescence imaging, we examined the cytotoxicity of **BS-CN** and **BS-MN** in live cells using a standard MTT assay. HeLa cells growing in log phase were seeded into 96-well plates and incubated with the two probes at different concentrations for 24 h. Based on the results of the MTT assay (Fig. S3†), no significant decrease in cell viability was observed after the addition of **BS-CN** or **BS-MN** for 24 h. **BS-CN** exhibited negligible cytotoxicity in HeLa cells, and **BS-MN** showed slightly lower cytotoxicity. Next, we performed fluorescence imaging experiments by CLSM. The commercial nuclear marker Hoechst 33342 was used to determine cellular uptake (Fig. S4†).[41] Living HeLa cells were stained with 500 nM **BS-CN**/**BS-MN** for 30 min, and bright filaments in the cytoplasm were distinctly observed only in the group stained with **BS-CN**. This phenomenon was observed in the group stained with **BS-MN** at 1 μM. This is because **BS-CN** had a higher fluorescence quantum yield than that of **BS-MN**. Based on our experience and previous reports, we speculate that **BS-CN**/**BS-MN** targets mitochondria in living cells. Owing to the spectral crosstalk between our probes and commercial MitoTracker Deep Red (MTDR), we evaluated this conjecture by co-staining experiments with commercial MTG (Mito-Tracker Green) in HeLa cells. As shown in Fig. 2, **BS-CN** and **BS-MN** overlapped well with MTG; the Pearson co-localization coefficients were 0.89 and 0.95 and the Manders' overlap coefficients were 0.97 and 0.99, respectively. These data revealed that the probes were located exclusively in the mitochondria of living cells.

3.4. The response of BS-CN and BS-MN to RNA

As shown in Fig. 2, **BS-CN** stained a small area of the nucleus. Therefore, we speculated that **BS-CN** may be RNA-selective. RNA titration experiments were conducted (Fig. 3E and F). As the RNA content increased, the fluorescence intensities of the two probes gradually increased and ultimately stabilized. After adding 9.5 μM and 16.4 μM RNA, the fluorescence intensities of **BS-CN** and **BS-MN** increased approximately 5.6 times and 16 times, respectively. These results indicate that **BS-CN** and **BS-MN** have affinity for RNA. The significant enhancement of fluorescence in **BS-MN** could be explained by the restriction of intramolecular rotation when **BS-MN** was bound to RNA.

As shown in Fig. S5,† the fluorescence intensities of **BS-CN** and **BS-MN** did not increase significantly in various cationic and anionic solutions, but were significantly enhanced in the RNA stock solution (1 mM, dissolved in PBS). This result indicated that the two probes had higher selectivity for RNA. Next, we conducted staining experiments on the fixed cells using the two probes. As shown in Fig. 3A and C, **BS-CN** and **BS-MN** stained the nucleoli and cytoplasm. We speculated that the two probes stained RNA in the fixed cells because RNA was mainly distributed in the cytoplasm and nucleoli. For **BS-CN**, the fluorescence intensity in the nucleoli of fixed cells was significantly higher than that in living cells. Compared with **BS-MN**, **BS-CN** stained the nucleolus more clearly and brightly. The cells

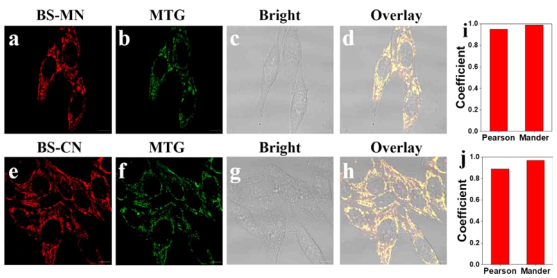

Fig. 2 Co-localization experiment. Images of 1 μM BS-MN (a) and 500 nM BS-CN (e) with 200 nM MTG (b and f) for 30 min; images of bright field (c and g) and overlayed (d and h); the Pearson's and Manders' coefficients of BS-MN (i) and BS-CN (j). Scale bar = 10 μm.

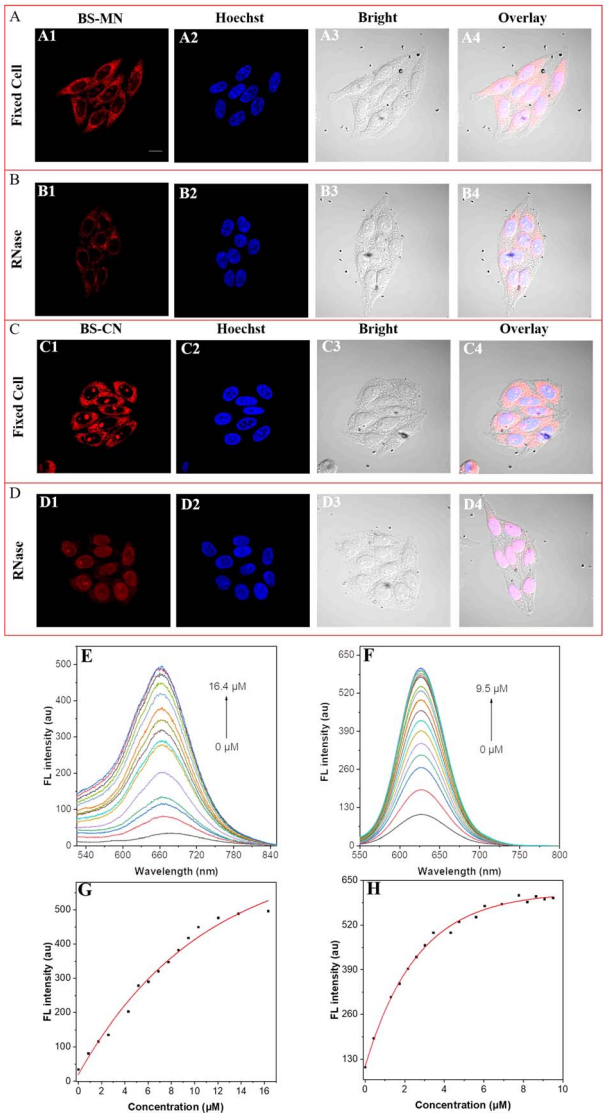

Fig. 3 Images of fixed HeLa cells untreated/treated with 5 mg mL^{-1} RNase for 2 h and then stained with 1 μM **BS-MN** (A and B)/500 nM **BS-CN** (C and D) for 30 min and 2 μM Hoechst for 10 min. (E and F) the emission spectra of **BS-MN** (E)/**BS-CN** (F) in the presence of different concentrations of RNA. (G and H) Fluorescence intensity of **BS-MN** (G)/**BS-CN** (H) dependent on the RNA concentration. Scale bar = 10 μm. FL: fluorescence.

were then treated with RNase and stained with **BS-CN** and **BS-MN** (Fig. 3B and D). **BS-CN** did not stain the nucleoli and cytoplasm but was localized in the nucleus, indicating that **BS-CN** binds to DNA in the nucleus only after RNA ablation. However, similar results were not obtained for **BS-MN**. Therefore, **BS-CN** may be used as a nucleolar probe. Furthermore, to demonstrate the abilities of **BS-CN** and **BS-MN** to bind RNA, we conducted molecular docking analyses. Due to the hydrogen bonding interactions, **BS-CN** exhibited better bonding ability than that of **BS-MN**, as evidenced by their docking free energies (-8.46 kcal mol^{-1} and -7.25 kcal mol^{-1}, respectively), as shown in Fig. S6.†

3.5. Photostability and long-time tracking ability of BS-CN and BS-MN

Photostability is a crucial property for fluorescence probes in bioimaging applications, especially in long-term tracking.[42] Photo-bleaching is a common problem in many organic fluorescence probes and limits the temporal monitoring of dynamic intracellular processes. To test the stability of the probes under continuous laser scanning, we performed imaging using CLSM for 40 min. As shown in Fig. 4A and B, after 40 min of laser scanning, **BS-CN** still had a higher fluorescence intensity than those of the two probes, whereas the fluorescence intensity of **BS-MN** decreased significantly. Our experiments demonstrated that **BS-CN** exhibited stronger anti-photobleaching ability than that of **BS-MN**.

To test the stability of both probes over extended periods, we performed imaging for various time intervals ranging from 1 to 60 h using 500 nM **BS-CN** and 1 μM **BS-MN**. As shown in Fig. 4C and D, both **BS-CN** and **BS-MN** maintained their high brightness for a long time while targeting the mitochondria of HeLa cells. In contrast, the fluorescence brightness of the commercial MTG decreased significantly over time (Fig. 4E). After 60 h of staining, we used these cells for co-localization experiments with **BS-CN** and **BS-MN** (Fig. S7†). Notably, both **BS-CN** and **BS-MN** displayed good overlap with MTG, with Pearson co-localization coefficients of 0.81 and 0.88, respectively. These findings highlight the relative stability of **BS-CN** and **BS-MN**, as they remained within the cells without being expelled during cellular metabolism. These probes may be helpful for high-

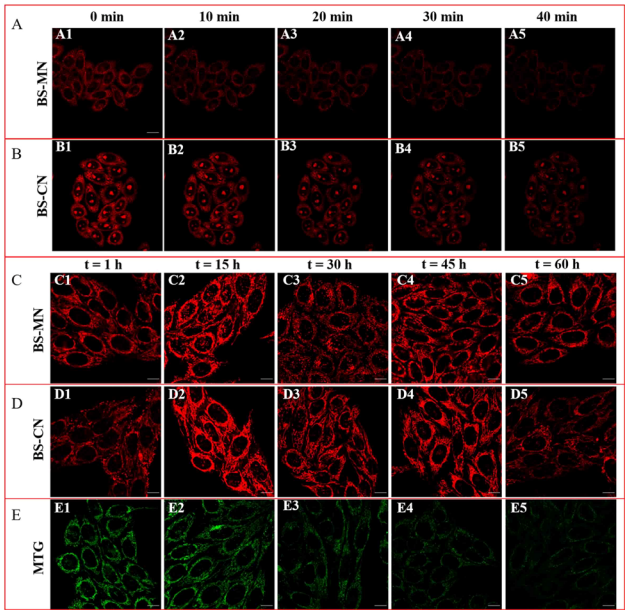

Fig. 4 (A and B) **BS-MN** and **BS-CN** were incubated for 30 min and obtained the images every ten minutes under continuous laser scanning. **BS-MN** (C), **BS-CN** (D) and MTG (E) were incubated for 1 h and then removed from the cell culture medium. Time-lapse images were acquired after 1, 15, 30, 45 and 60 h of staining in HeLa cells. **BS-MN**: 1 μM; **BS-CN**: 500 nM; MTG: 200 nM. Scale bar = 10 μm.

resolution and delayed mitochondrial monitoring in future research.

4. Conclusion

In summary, we designed and synthesized fluorescence probes, **BS-MN** and **BS-CN**, using a strategy for conferring rigidity through intramolecular esterification to improve the molecular structure. **BS-CN**, based on benzo[*h*]coumarin, exhibited a higher photobleaching resistance and fluorescence quantum yield and lower staining concentration than those of **BS-MN**. Both probes exhibited precise mitochondrial targeting in live cells, enabling long-term tracking and imaging for up to 60 h. Importantly, after cell fixation, the mitochondrial membrane potential diminished, causing the migration of **BS-CN** from the mitochondria to the nucleoli and allowing for clear staining of the nucleoli. In conclusion, these two probes serve as powerful tools for the long-term tracking of mitochondria in live cells, and **BS-CN** may be an effective nucleolar probe for tissue imaging.

Author contributions

Chengjing Zhang: conceptualization, methodology, investigation, data curation, writing–original draft. Zihao Yu: investigation, data curation. Yang Liu: investigation, data curation, formal analysis. Wendong Jin: data curation, investigation. Zhiqiang Liu: resources, funding acquisition, supervision, writing–review & editing. Xiaoqiang Yu: resources, funding acquisition, writing–review & editing.

Conflicts of interest

There are no conflicts to declare.

Acknowledgements

This work was supported by National Natural Science Foundation of China (U2330106 and 52350002), and the Fundamental Research Funds for the Central Universities (2022JC003).

References

1 H. Cheng, Y. Li, B. Tang and J. Yoon, *Chem. Soc. Rev.*, 2020, **49**, 21–31.
2 T. Kowada, H. Maeda and K. Kikuchi, *Chem. Soc. Rev.*, 2015, **44**, 4953–4972.
3 G. Lukinavičius, L. Reymond, E. D'Este, A. Masharina, F. Göttfert, H. Ta, A. Güther, M. Fournier, S. Rizzo, H. Waldmann, C. Blaukopf, C. Sommer, D. Gerlich, H. Arndt, S. Hell and K. Johnsson, *Nat. Methods*, 2014, **11**, 731–733.
4 Y. Xu, R. Xu, Z. Wang, Y. Zhou, Q. Shen, W. Ji, D. Dang, L. Meng and B. Tang, *Chem. Soc. Rev.*, 2021, **50**, 667–690.
5 L. Wu, J. Liu, P. Li, B. Tang and T. James, *Chem. Soc. Rev.*, 2021, **50**, 702–734.
6 X. Liu, B. Yu, Y. Shen and H. Cong, *Coord. Chem. Rev.*, 2022, **468**, 214609.
7 J. Lin, K. Yang and E. J. New, *Org. Biomol. Chem.*, 2021, **19**, 9339–9357.
8 Y. Huang, Y. Zhang, F. Huo, Y. Wen and C. Yin, *Sci. China: Chem.*, 2020, **63**, 1742–1755.
9 G. Niu, W. Liu, H. Xiao, H. Zhang, J. Chen, Q. Dai, J. Ge, J. Wu and P. Wang, *Chem.–Asian J.*, 2016, **11**, 498–504.
10 Y. W. Jun, H. R. Kim, Y. J. Reo, M. Dai and K. H. Ahn, *Chem. Sci.*, 2017, **8**, 7696–7704.
11 N. I. Georgiev, V. V. Bakov, K. K. Anichina and V. B. Bojinov, *Pharmaceuticals*, 2023, **16**, 381.
12 C. Zong, Q. Lu, J. Niu, F. Meng and X. Yu, *Spectrochim. Acta, Part A*, 2023, **299**, 122883.
13 S. Wang, W. X. Ren, J. T. Hou, M. Won, J. An, X. Chen, J. Shu and J. S. Kim, *Chem. Soc. Rev.*, 2021, **50**, 8887–8902.
14 Q. Wang, Z. Li, Y. Hao, Y. Zhang and C. Zhang, *Anal. Chem.*, 2022, **94**, 17328–17333.
15 L. Guo, M. Tian, Z. Zhang, Q. Lu, Z. Liu, G. Niu and X. Yu, *J. Am. Chem. Soc.*, 2021, **143**, 3169–3179.
16 S. Fulda, L. Galluzzi and G. Kroemer, *Nat. Rev. Drug Discovery*, 2010, **9**, 447–464.
17 L. Galluzzi and G. Kroemer, *Cell*, 2008, **135**, 1161–1163.
18 M. Khacho, R. Harris and R. S. Slack, *Nat. Rev. Neurosci.*, 2018, **20**, 34–48.
19 X. Zhang, Q. Sun, Z. Huang, L. Huang and Y. Xiao, *J. Mater. Chem. B*, 2019, **7**, 2749–2758.
20 A. M. Aleardi, G. Benard, O. Augereau, M. Malgat, J. C. Talbot, J. P. Mazat, T. Letellier, J. Dachary-Prigent, G. C. Solaini and R. Rossignol, *J. Bioenerg. Biomembr.*, 2005, **37**, 207–225.
21 W. Liu, Q. Qiao, J. Zheng, J. Chen, W. Zhou, N. Xu, J. Li, L. Miao and Z. Xu, *Biosens. Bioelectron.*, 2021, **176**, 112886.
22 X. Li, J. Zheng, W. Liu, Q. Qiao, J. Chen, W. Zhou and Z. Xu, *Chin. Chem. Lett.*, 2020, **31**, 2937–2940.
23 Z. Lv, Z. Man, H. Cui, Z. Xu, H. Cao, S. Li, Q. Liao, Q. He, L. Zheng and H. Fu, *Adv. Funct. Mater.*, 2021, **31**, 2009329.
24 L. D. Zorova, V. A. Popkov, E. Y. Plotnikov, D. N. Silachev, I. B. Pevzner, S. S. Jankauskas, V. A. Babenko, S. D. Zorov, A. V. Balakireva, M. Juhaszova, S. J. Solott and D. B. Zorov, *Anal. Biochem.*, 2018, **552**, 50–59.
25 J. Niu, S. Yang, M. Tian and X. Yu, *Sens. Actuators, B*, 2022, **372**, 132693.
26 M. Y. Wu, K. Li, Y. H. Liu, K. K. Yu, Y. M. Xie, X. D. Zhou and X. Q. Yu, *Biomaterials*, 2015, **53**, 669–678.
27 W. Niu, L. Guo, Y. Li, S. Shuang, C. Dong and M. S. Wong, *Anal. Chem.*, 2016, **88**, 1908–1914.
28 F. Miao, W. Zhang, Y. Sun, R. Zhang, Y. Liu, F. Guo, G. Song, M. Tian and X. Yu, *Biosens. Bioelectron.*, 2014, **55**, 423–429.
29 P. S. Deore, D. S. Coman and R. A. Manderville, *Chem. Commun.*, 2019, **55**, 3540–3543.
30 C. Y. Y. Yu, W. Zhang, R. T. K. Kwok, C. W. T. Leung, J. W. Y. Lam and B. Z. Tang, *J. Mater. Chem. B*, 2016, **4**, 2614–2619.
31 M. Tian, J. Sun, B. Dong and W. Lin, *Sens. Actuators, B*, 2019, **292**, 16–23.

32 T. Liu, T. Stephan, P. Chen, J. Keller-Findeisen, J. Chen, D. Riedel, Z. Yang, S. Jakobs and Z. Chen, *Proc. Natl. Acad. Sci. U. S. A.*, 2022, **119**, e2215799119.
33 M. Ishigaki, M. Iketani, M. Sugaya, M. Takahashi, M. Tanaka, S. Hattori and I. Ohsawa, *Mitochondrion*, 2016, **28**, 79–87.
34 F. Chen, W. Liu, H. Li, T. Deng, B. Xing and F. Liu, *Analysis Sensing*, 2022, **2**, e202100066.
35 G. Zhang, Y. Sun, X. He, W. Zhang, M. Tian, R. Feng, R. Zhang, X. Li, L. Guo, X. Yu and S. Zhang, *Anal. Chem.*, 2015, **24**, 12088–12095.
36 R. Yang, X. He, G. Niu, F. Meng, Q. Lu, Z. Liu and X. Yu, *ACS Sens.*, 2021, **6**, 1552–1559.
37 L. Guo, H. Liu, X. Jin, Z. Zhang, J. Su and X. Yu, *Sens. Actuators, B*, 2021, **341**, 129962.
38 J. Fu, J. Niu, Q. Hao, F. Meng, C. Zong, X. He, Z. Liu and X. Yu, *Dyes Pigm.*, 2023, **216**, 111352.
39 H. Xiong, L. He, Y. Zhang, J. Wang, X. Song and Z. Yang, *Chin. Chem. Lett.*, 2019, **30**, 1075–1077.
40 Z. Fang, Y. Wang and Y. Wang, *Org. Lett.*, 2019, **21**, 434–438.
41 M. Cao, T. Zhu, M. Zhao, F. Meng, Z. Liu, J. Wang, G. Niu and X. Yu, *Anal. Chem.*, 2022, **94**, 10676–10684.
42 K. Devarajan, M. Sivakalai, S. M. Basu, C. Biswas, M. Chauhan, U. Hasan, Y. Panneerselvam, U. M. Narayanan, S. S. K. Raavi, J. Giri and T. K. Panda, *Biomater. Sci.*, 2023, **11**, 3938–3951.